Electrical and Computer Engineering Faculty Research & Creative Works

Electrical and Computer Engineering

01 Jan 1996

# A Hybrid Observer for High Performance Brushless DC Motor Drives

Keith Corzine
*Missouri University of Science and Technology*

S. D. Sudhoff

## Recommended Citation

# A HYBRID OBSERVER FOR HIGH PERFORMANCE
# BRUSHLESS DC MOTOR DRIVES

K. A. Corzine, Student Member                                    S. D. Sudhoff, Member

Department of Electrical Engineering
University of Missouri - Rolla
Rolla, Missouri 65401

*Abstract* - Brushless DC drive systems are used in a wide variety of applications. These drives may be classified as being one of two types; sinusoidal drives in which there are no low-frequency harmonics in the current waveforms and no low-frequency torque ripple and non-sinusoidal drives in which there is considerable low-frequency harmonic content, both in the current and torque waveforms. Although the sinusoidal drives feature superior performance, they are generally more expensive since rotor position must be sensed on a continuous basis, thus requiring an optical encoder or a resolver, whereas relatively inexpensive Hall-effect sensors may be used for non-sinusoidal drives. In this paper, a straightforward hybrid observer is set forth which enables rotor position to be estimated on a continuous basis using information available from the Hall-effect sensors. The proposed observer is experimentally shown to perform just as well as an optical encoder for steady-state conditions and nearly as well as the optical encoder during transient conditions. The proposed scheme provides designers with a new option for rotor position sensing, one which offers an excellent compromise between accuracy and expense.

## I. INTRODUCTION

Brushless DC drive systems are used in a wide variety of applications including computer disk drives, robotics, actuators, electric vehicles, and, most recently, ship propulsion. For certain applications, such as fan loads, low frequency torque ripple is acceptable. An example of a drive which exhibits low frequency torque ripple is the 180° voltage source inverter which uses relatively inexpensive Hall-effect devices to sense rotor position. Using a 120° voltage source inverter and eliminating the Hall-effect devices by sensing rotor position from the back EMF waveform can further reduce the cost [1]. However, low-frequency torque pulsations are not acceptable for many applications. For these applications high performance sinusoidal type drives are needed. These drives produce nearly constant torque but require a resolver or an optical encoder to measure the rotor position accurately. The encoder or resolver can increase the cost of the drive by $300 to $3000 depending on the application. This cost is further increased by the fact that an added frame is needed to house the encoder/resolver and the installation cost can be $100 to $1000. The cost of calibration is small (< $100) since it can usually by accomplished in software. Although methods have been proposed to operate high-performance drives using an

inexpensive observer instead of a resolver or encoder, these methods require an elaborate scheme for start up [2], and cannot guarantee a bound on the initial estimation error. Furthermore, these methods generally require knowledge of the machine parameters.

This paper sets forth a straightforward and easily implemented hybrid observer algorithm which allows the operation of sinusoidal type brushless DC drives from Hall-effect devices which cost about $1.50. The installation cost is < $100 since the hall effect sensors can be built into the stator. Calibration can usually be accomplished in software and is thus a small cost (< $100). No special provisions are required for start up and transient operation, and knowledge of the machine parameters is not required. Furthermore, the error in the estimation of the rotor position is bounded by a limit which is independent of operating conditions.

## II. SYSTEM DESCRIPTION

Fig 1. illustrates an example of a high-performance brushless DC drive system used to demonstrate the hybrid observer set forth herein. In addition to the machine and inverter, the system includes a speed control and a delta-modulated current control. The speed control calculates the commanded q- and d-axis currents, $i_{qs}^{r*}$ and $i_{ds}^{r*}$, such that the observed speed $\hat{\omega}_r$ will become equal to the commanded speed $\omega_r^*$. The reference frame transformation is used to map the qd current command into the corresponding machine variable current command $i_{as}^*$, $i_{bs}^*$, and $i_{cs}^*$, a process which requires knowledge of the rotor position or the sine and cosine of the rotor position. The delta-modulated current control compares the commanded currents to
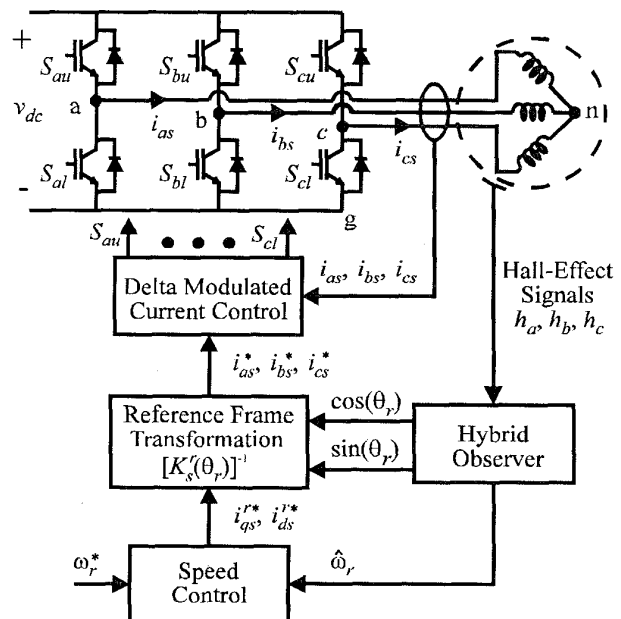


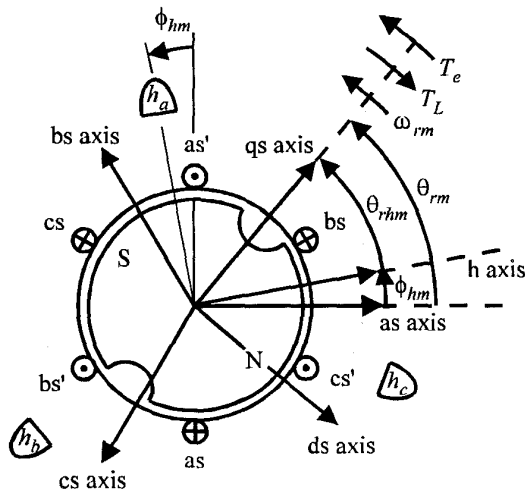Figure 1. High-performance brushless DC machine drive.

Figure 2. Permanent-magnet synchronous machine.

the actual currents of the machine, $i_{as}$, $i_{bs}$, and $i_{cs}$, and switches the inverter transistors in such a way that the commanded currents are obtained. Each component of the example drive system is described in detail in the following paragraphs.

Fig. 2 illustrates a 2-pole 3-phase permanent-magnet synchronous machine. Therein, each lumped winding actually represents a sinusoidally distributed winding. The mechanical rotor position relative to the as-axis and the mechanical rotor speed are denoted $\theta_{rm}$ and $\omega_{rm}$, respectively. Three Hall-effect position sensors, labeled $h_a$, $h_b$, and $h_c$, are spatially located $\pi/P$, $5\pi/3P$, and $9\pi/3P$ radians counterclockwise from the h-axis, where P is the number of poles. As can be seen the h-axis is displaced from the as-axis by $\phi_{hm}$. Mechanical rotor position relative to the h-axis, that is the mechanical rotor position relative to the Hall-effect devices, is denoted $\theta_{rhm}$. It is convenient to define the electrical rotor position and speed, $\theta_r$ and $\omega_r$, the electrical rotor position relative to the Hall-effect sensors, $\theta_{rh}$ and the electrical displacement between the h- and as-axis, $\phi_h$ as $P/2$ times the corresponding mechanical quantities.

For the system investigated herein the machine is of the surface-mounted magnet type and has a sinusoidal back emf. Assuming that the effects of magnetic saturation of the stator iron as well as eddy currents are negligible, and that the machine is wye-connected, the quadrature and direct axis voltage equations of the permanent-magnet synchronous machine may be expressed [3]

$$v_{qs}^r = r_s i_{qs}^r + \omega_r L_{ss} i_{ds}^r + \omega_r \lambda_m' + L_{ss}\frac{di_{qs}^r}{dt} \tag{1}$$

$$v_{ds}^r = r_s i_{ds}^r - \omega_r L_{ss} i_{qs}^r + L_{ss}\frac{di_{ds}'}{dt} \tag{2}$$

where $r_s$, $L_{ss}$, and $\lambda_m'$ denote the stator resistance, stator self inductance (the leakage inductance plus 3/2 times the magnetizing inductance), and the flux linkage due to the permanent magnet, respectively. It can be shown that in terms of qd variables

$$T_e = \frac{3}{2}\frac{P}{2}\lambda_m' i_{qs}^r \tag{3}$$

In (1-3) the qd variables are related to machine variables by

$$f_{qd0s}^r = K_s^r(\theta_r) f_{abcs} \tag{4}$$

where

$$K_s^r(\theta_r) = \frac{2}{3}\begin{bmatrix} \cos(\theta_r) & \cos\left(\theta_r - \frac{2\pi}{3}\right) & \cos\left(\theta_r + \frac{2\pi}{3}\right) \\ \sin(\theta_r) & \sin\left(\theta_r - \frac{2\pi}{3}\right) & \sin\left(\theta_r + \frac{2\pi}{3}\right) \\ \frac{1}{2} & \frac{1}{2} & \frac{1}{2} \end{bmatrix} \tag{5}$$

and

$$f_{qd0s}^r = [\, f_{qs}^r \quad f_{ds}^r \quad f_{0s}^r \,]^T \tag{6}$$

$$f_{abcs} = [\, f_{as} \quad f_{bs} \quad f_{cs} \,]^T. \tag{7}$$

In (4-7), $f$ may be a voltage, current, or flux linkage. Since the machine is wye-connected, all zero sequence variables are zero and thus the zero sequence voltage equation is not listed. Although this model cannot be applied to every permanent magnet synchronous machine, it is sufficient for many drive systems. In the event that a more detailed machine model is needed, the reader is referred to [4].

From (3), it can be seen that a q-axis current command may be readily formulated in terms of qd variables, a fact upon which the speed control block diagram, shown in Fig. 3, is based. Therein the torque command is made up of a term proportional to the filtered speed error and to a term proportional to the integral of the speed error. Using (3), the torque command is translated into a q-axis current command. The d-axis current command is set to zero for the system herein, however for high speed operation flux-weakening strategies such as that set forth in [5] may be used.

The machine variable current command, $i^*_{abcs}$, is found in terms of the q- and d-axis current command using (4). From (5) it is apparent that this requires knowledge of either $\theta_r$ or $\sin(\theta_r)$ and $\cos(\theta_r)$ (the other trigonometric functions in (5) may be readily expressed in terms of $\sin(\theta_r)$ and $\cos(\theta_r)$).

The delta-modulated current control governs the switching of the six inverter valves such that the actual currents $i_{abcs}$ are held near the currents commanded by the speed control. The state diagram of the delta-modulated control strategy is depicted in Fig. 4. As can be seen, there are two switching states for each leg, either $S_{xu}$ is on and $S_{xl}$ is off (the positive state), or $S_{xu}$ is off and $S_{xl}$ is on (the negative state), where x may be 'a','b', or 'c'. The delta-modulated circuit is clocked at a constant frequency. If $i_{xs} < i^*_{xs}$ when the circuit is clocked then a state transition is made to the positive state. Conversely, if $i_{xs} > i^*_{xs}$ when the circuit is clocked, a transition is made to the negative state. Using this type of control with a sufficiently high switching frequency will yield actual currents which closely track the commanded currents. This method has an advantage over the hysteresis current-regulated control [5-6] in that the switching frequency is fixed and does not depend on the load or operating point.

The system presented herein is an example to demonstrate the use of the hybrid observer. As will be shown, the observer makes no use of any of the machine or drive parameters. Thus it can be used with any type of control strategy on any type of machine in which it is desirable to know the rotor position.

## III. HYBRID ROTOR POSITION OBSERVER

The hybrid observer set forth in this section is based on the differential equation

$$\frac{d}{dt}\begin{bmatrix} \cos(\theta_{rh}) \\ \sin(\theta_{rh}) \end{bmatrix} = \begin{bmatrix} 0 & -\omega_r \\ \omega_r & 0 \end{bmatrix}\begin{bmatrix} \cos(\theta_{rh}) \\ \sin(\theta_{rh}) \end{bmatrix} \tag{8}$$

If the initial rotor position and exact electrical rotor speed are known, and if (8) could be solved numerically with no error, the sine and cosine of the electrical rotor position relative to the Hall-effect sensors,
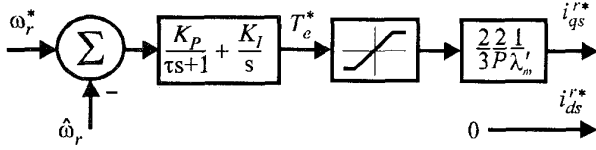
Figure 3. Speed control block diagram.

$\sin(\theta_{rh})$ and $\cos(\theta_{rh})$, could be determined, whereupon $\sin(\theta_r)$ and $\cos(\theta_r)$ could be determined using trigonometric identities. Unfortunately, there are no means to determine either the initial rotor position or the exact electrical rotor speed. Nevertheless, (8) can still be used to accurately determine $\sin(\theta_{rh})$ and $\cos(\theta_{rh})$, provided that it is augmented with information which is available from the Hall-effect sensors. In particular, information from the Hall-effect sensors can be used to (i) determine limits on $\sin(\theta_h)$ and $\cos(\theta_h)$ thus bounding the error in the estimation of these quantities, (ii) determine the exact value of $\sin(\theta_{rh})$ and $\cos(\theta_{rh})$ whenever there is a transition of one of the outputs of the Hall-effect sensors, and (iii) estimate electrical rotor speed based on the length of time which passes between Hall-effect sensor transitions.

Fig. 5 illustrates the use of the Hall-effect devices to bound the estimates for $\sin(\theta_{rh})$ and $\cos(\theta_{rh})$. Therein, the first three traces depict the output of the Hall-effect sensors as a function of electrical rotor position relative to the Hall-effect sensors. The next trace illustrates $\sin(\theta_{rh})$, the maximum value of $\sin(\theta_{rh})$ possible for the current Hall-effect sensor state, denoted $\text{maxsin}(h_a, h_b, h_c)$, and the minimum value of $\sin(\theta_{rh})$ possible for the current Hall-effect sensor state, denoted $\text{minsin}(h_a, h_b, h_c)$. The calculation of these functions is based upon the fact that for a given Hall-effect state the electrical rotor position is known to within a $\pi/3$ interval. The next trace illustrates $\cos(\theta_{rh})$ as well as its bounding functions which are denoted $\text{maxcos}(h_a, h_b, h_c)$ and $\text{mincos}(h_a, h_b, h_c)$. The bounding functions are enumerated in Table 1.

Table 1. Bounding Functions vs. Hall State

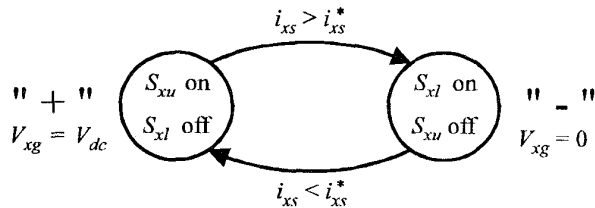| Hall State | | | Bounding Functions | | | |
|---|---|---|---|---|---|---|
| $h_a$ | $h_b$ | $h_c$ | $\text{maxsin}(\theta_h)$ | $\text{minsin}(\theta_h)$ | $\text{maxcos}(\theta_h)$ | $\text{mincos}(\theta_h)$ |
| 0 | 0 | 1 | -1/2 | -1 | 0 | $-\sqrt{3}/2$ |
| 0 | 1 | 0 | 1 | 1/2 | 0 | $-\sqrt{3}/2$ |
| 0 | 1 | 1 | 1/2 | -1/2 | $-\sqrt{3}/2$ | -1 |
| 1 | 0 | 0 | 1/2 | -1/2 | 1 | $\sqrt{3}/2$ |
| 1 | 0 | 1 | -1/2 | -1 | $\sqrt{3}/2$ | 0 |
| 1 | 1 | 0 | 1 | 1/2 | $\sqrt{3}/2$ | 0 |



Figure 4. State transition diagram for one leg of delta-modulated controlled inverter.

At the points at which a Hall-effect transition occurs the minimum and maximum bounding functions converge, so that at these points the exact values of $\sin(\theta_{rh})$ and $\cos(\theta_{rh})$ are known. For example, given that Hall-effect sensor $h_a$ has undergone a high-to-low transition, the rotor position is either $\pi/2$ if the rotor speed is positive or $3\pi/2$ if the rotor speed is negative. In order to avoid reliance on the knowledge of rotor speed, the other Hall effect sensors can be used. For example, if $h_b$ is high and $h_c$ is low during a transition of $h_a$, then at that point $\theta_{rh} = \pi/2$. Thus it can be seen that, at each transition point, the exact value of $\theta_{rh}$ is known. Table 2 lists the Hall-effect transition points along with the corresponding values of $\sin(\theta_{rh})$ and $\cos(\theta_{rh})$.

Table 2. State Transition Points

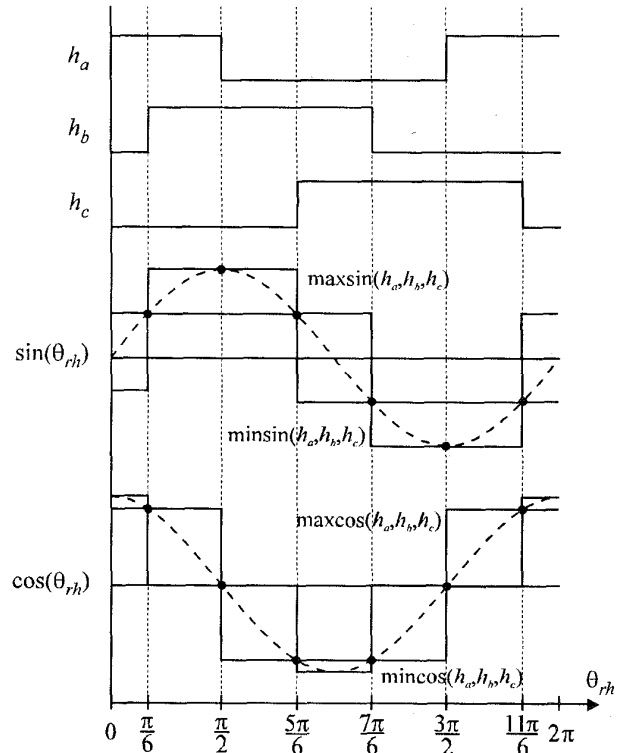| Sensor Transition | $h_a$ | $h_b$ | $h_c$ | $\sin(\theta_{rh})$ | $\cos(\theta_{rh})$ |
|---|---|---|---|---|---|
| $h_a$ | x | 0 | 1 | -1 | 0 |
| $h_a$ | x | 1 | 0 | 1 | 0 |
| $h_b$ | 0 | x | 1 | -1/2 | $-\sqrt{3}/2$ |
| $h_b$ | 1 | x | 0 | 1/2 | $\sqrt{3}/2$ |
| $h_c$ | 0 | 1 | x | 1/2 | $-\sqrt{3}/2$ |
| $h_c$ | 1 | 0 | x | -1/2 | $\sqrt{3}/2$ |
| x = irrelevant | | | | | |



Figure 5. Hybrid observer bounding functions.

On each occurrence of a Hall-effect transition, the rotor speed can be estimated based on the time which has elapsed since the previous Hall-effect transition. In particular,

$$\hat{\omega}_r = \frac{\Delta\theta_{rh}}{\Delta t} \qquad (9)$$

where $\Delta\theta_{rh}$ is calculated based upon the rotor position corresponding to the current and previous Hall-effect transitions. Prior to the first Hall-effect transition, the estimated electrical rotor speed is taken to be zero, and at the first Hall-effect transition the previous rotor position (since there is no previous Hall-effect transition) is taken to be the midpoint value of $\Delta\theta_{rh}$ for the initial Hall-effect state.

Combining (8) with the information which can be deduced from the Hall effect states yields the hybrid observer depicted in Fig. 6 . Therein, $\hat{\omega}_r$ denotes the estimated electrical rotor speed, and $s_{\theta h}$ and $c_{\theta h}$ are the estimated values of $\sin(\theta_{rh})$ and $\cos(\theta_{rh})$ respectively. As can be seen, the structure of the control is based on (8), however, each of the integrators is subject to a variable limit which is a function of the Hall-effect state ($h_a$, $h_b$, and $h_c$) as described in Table 1. In addition, every time a transition in Hall-effect state occurs the integrators are reset to the value specified in Table 2.

One final calculation is necessary to implement the proposed Hybrid observer. In particular, a method is set forth to determine the sine and cosine of electrical rotor position relative to the as-axis, which is required to make the reference frame transformation, instead of the electrical rotor position relative to the Hall-effect sensors. Since

$$\theta_r = \theta_{rh} + \phi_h \qquad (10)$$

it follows that

$$\sin(\theta_r) = \sin(\theta_{rh})\cos(\phi_h) + \cos(\theta_{rh})\sin(\phi_h) \qquad (11)$$

$$\cos(\theta_r) = \cos(\theta_{rh})\cos(\phi_h) - \sin(\theta_{rh})\sin(\phi_h) \qquad (12)$$

Thus, it terms of the estimated values for $\sin(\theta_{rh})$ and $\cos(\theta_{rh})$

$$\sin(\theta_r) = s_{\theta h}\cos(\phi_h) + c_{\theta h}\sin(\phi_h) \qquad (13)$$

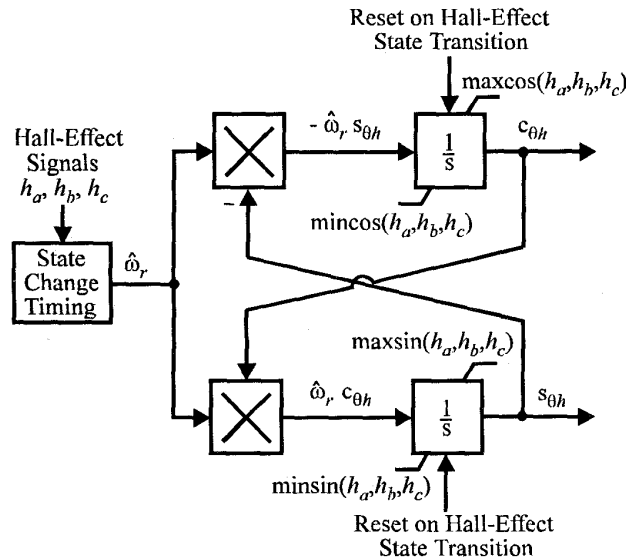$$\cos(\theta_r) = c_{\theta h}\cos(\phi_h) - s_{\theta h}\sin(\phi_h) \qquad (14)$$

The initial conditions for the Hall-effect observer are straightforward. Initially, it is assumed that the electrical rotor speed is zero. The initial conditions for $s_{\theta h}$ and $c_{\theta h}$ are determined from the initial Hall-effect sensor readings. In particular, the initial conditions are chosen to be in the center of the interval over which the current Hall-effect state is constant, as listed in Table 3. In so doing, the maximum possible error in the initial rotor position estimate is $\pi/6$.

### Table 3. Initial Conditions

| Initial Hall State | | | Initial Conditions | | |
|---|---|---|---|---|---|
| $h_a$ | $h_b$ | $h_c$ | $\theta_h$ | $s_{\theta h}$ | $c_{\theta h}$ |
| 0 | 0 | 1 | $4\pi/3$ | $-\sqrt{3}/2$ | $-1/2$ |
| 0 | 1 | 0 | $2\pi/3$ | $\sqrt{3}/2$ | $-/2$ |
| 0 | 1 | 1 | $\pi$ | 0 | $-1$ |
| 1 | 0 | 0 | 0 | 0 | 1 |
| 1 | 0 | 1 | $5\pi/3$ | $-\sqrt{3}/2$ | $1/2$ |
| 1 | 1 | 0 | $\pi/3$ | $\sqrt{3}/2$ | $1/2$ |

As a final note, there are two extensions of the method which may be useful in certain applications. First, the method may be modified for use with any number of Hall-effect sensors. Fewer sensors can be used if cost is to be further reduced or more can be used if the maximum possible error is to be decreased. The second modification of the method is to account for situations in which the Hall-effect sensors are not evenly spaced. In either case, the only modifications necessary are the reconstruction of Tables 1, 2, and 3 so as to correspond to the new mechanical layout.

### IV. STEADY-STATE PERFORMANCE

The hybrid observer set forth in the previous section will be demonstrated both experimentally and through the use of computer simulation by comparing the performance of the test system using the hybrid observer with that of the same system using an optical encoder. The test system consists of a 4-pole 3/4 hp machine with $r_s = 2.99\ \Omega$, $L_{SS} = 11.35$ mH, and $\lambda'_m = 0.156$ V·sec/rad. Separate magnets on the rotor shaft were used to excite the Hall-effect sensors. The inverter was operated at $v_{dc} = 196.9$ V with a delta-modulation control clock frequency of $f_c = 15.3$ kHz. It was observed that the IGBT and diode forward voltage drops were 1.7 and 1.0 volts respectively. The IGBT turn on and turn off times were 400 ns and 600 ns, and a deadtime of 2.0 $\mu$sec was used to avoid shoot through.

Figs. 7 and 8 illustrate system performance the hybrid observer and optical encoder, respectively. For this study, the machine is operating at a constant speed of $\omega_{rm} = 555.1$ rad/sec. The speed control is disabled and the commanded q- and d-axis currents are $i_{qs}^{r*} = 3.0$ A and $i_{ds}^{r*} = 0$. In both figures the a-phase stator current as measured in the laboratory, the a-phase current obtained from the computer simulation, and the electromagnetic torque from the computer simulation are shown. The computer simulation of the current waveform is intended to provide verification of the simulation, which was used in order to determine the instantaneous torque waveform in lieu of the measured torque waveform since the appropriate equipment was not available. Further verification of the simulation appears in [5,6]. As can be seen, there is little difference in the steady-state performance between the hybrid observer and
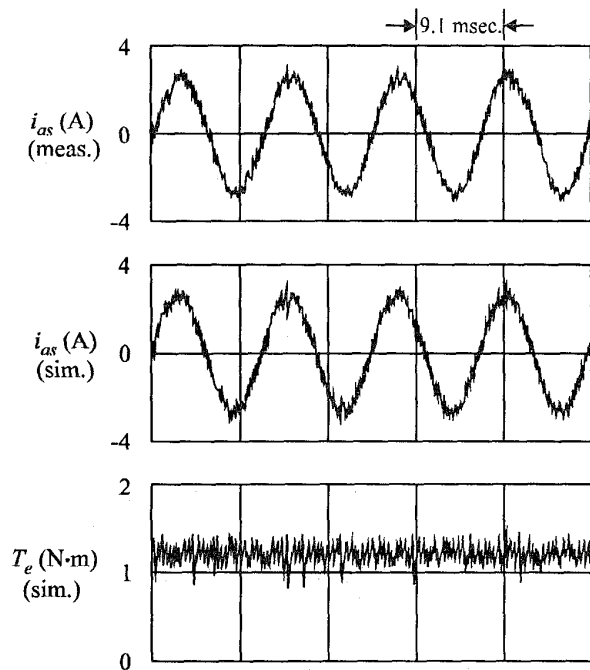


Figure 6. Hybrid observer block diagram.

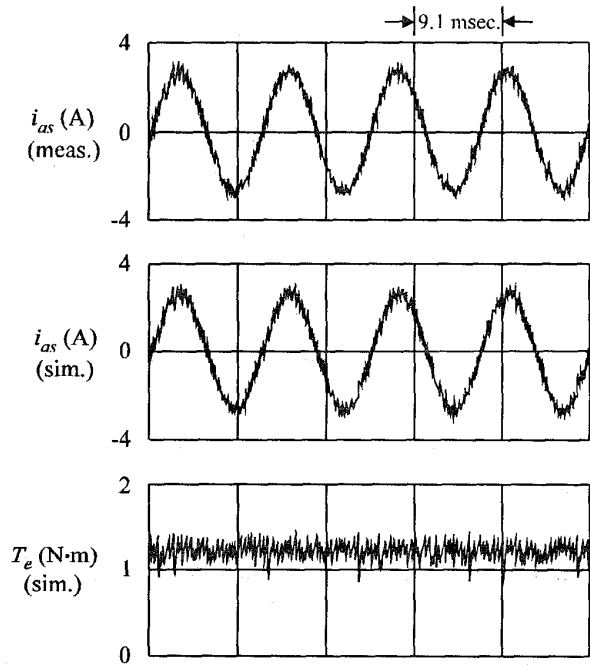Figure 7. Steady-state operation using the hybrid observer.



Figure 8. Steady-state operation using an optical encoder.

12-bit optical encoder based systems. In each case, the fundamental component of the current is a sinusoid upon which high-frequnecy switching harmonics are superimposed. The torque waveform is essentially constant other than the high-frequency ripple due to the switching of the inverter semiconductors, which has little-impact on drive operation.

## V. TRANSIENT PERFORMANCE

In this section, transient operation of the hybrid observer based brushless DC drive system is demonstrated during start up. The speed control is used with a commanded speed of $\omega^*_{rm} = 209.44$ rad/sec and proportional and integral gains of $K_P = 0.008$ N·m·sec and $K_I = 0.002$ N·m. The commanded torque is limited to 1.5 N·m, the speed error filter time constant is $\tau = 12.4$ msec, and the DC voltage was set to $v_{dc} = 141.0$ V. The Hall-effect displacement is $\phi_h = -2.75$ rad.

Figs. 9 and 10 show the measured a-phase current and rotor mechanical speed of the drive system using the hybrid observer and an optical encoder respectively. As can be seen, there is little difference in the start up performance of the hybrid observer based and the optical encoder based drives, although the hybrid drive does initially exhibit some discontinuity in the a-phase current waveform due to integral resets in the hybrid observer algorithm. The discontinuous current causes torque ripple which manifest itself in the
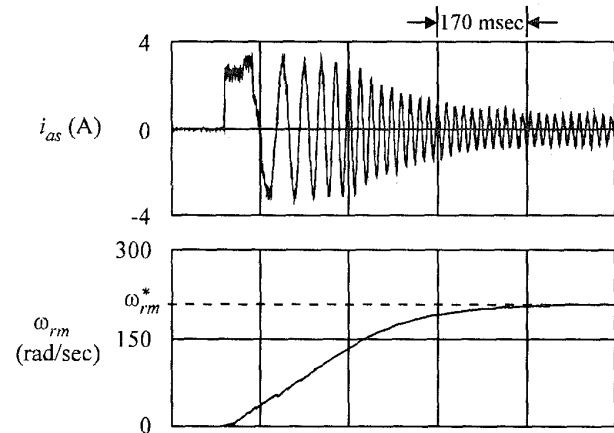


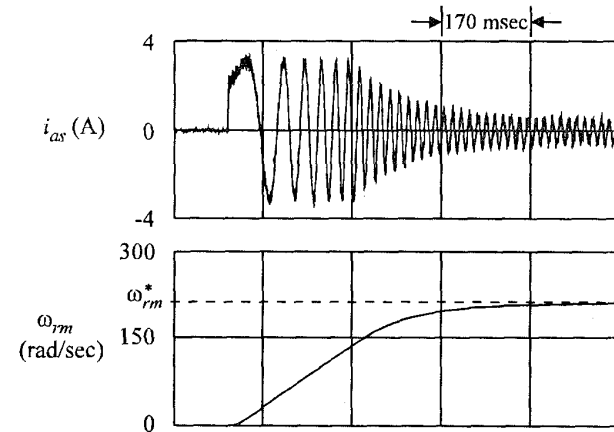Figure 9. Start up performance using the hybrid observer.



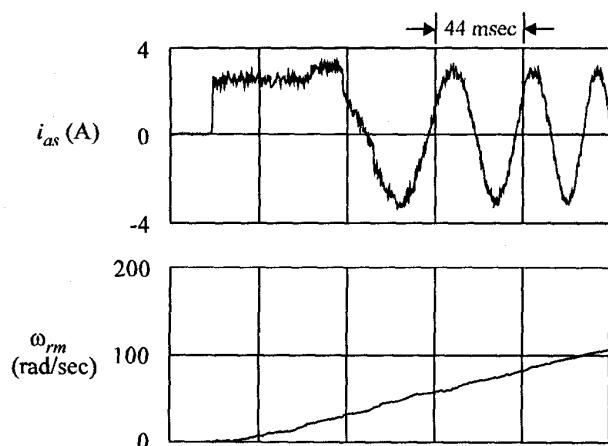Figure 10. Start up performance using an optical encoder.

4

$i_{as}$ (A)   0

-4

→| 44 msec |←

200

$\omega_{rm}$
(rad/sec)   100

0

Figure 11. Start up performance using the hybrid observer. Initial rotor position: $\theta_{rh} = 3\pi/2$.

4

$i_{as}$ (A)   0

-4

→| 44 msec |←

200

$\omega_{rm}$
(rad/sec)   100

0
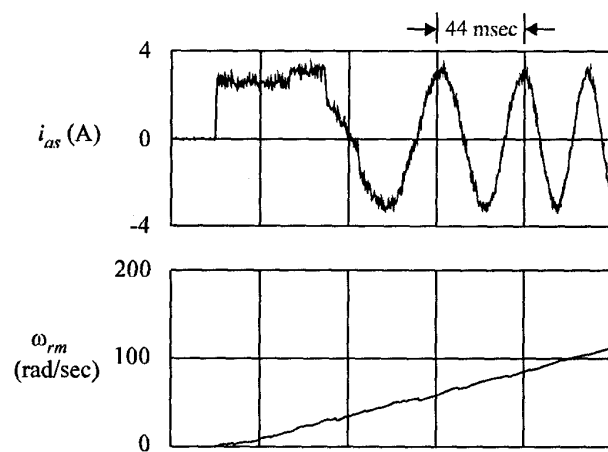
Figure 12. Start up performance using the hybrid observer. Initial rotor position: $\theta_{rh} = 5\pi/3$.

4

$i_{as}$ (A)   0

-4

→| 44 msec |←
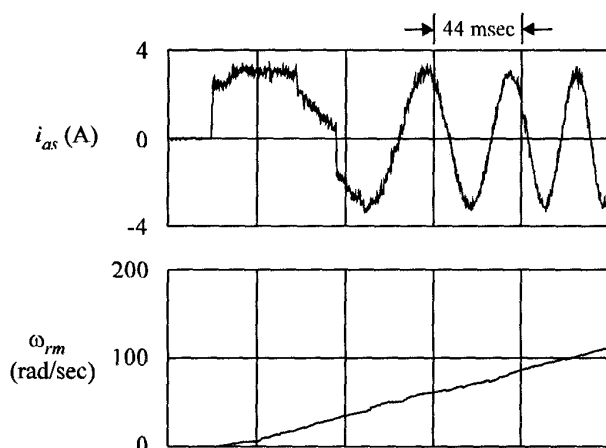
200

$\omega_{rm}$
(rad/sec)   100

0

Figure 13. Start up performance using the hybrid observer. Initial rotor position: $\theta_{rh} = 11\pi/6$.

speed waveform. However, the discontinuities in the current waveforms quickly subside even though the speed is still increasing and the estimated speed is not as accurate as in the steady-state. It should be noted that the ripple in the speed waveform is due to transient operation and not a result of low speed operation. The observer will operate without speed ripple at low speeds in the steady-state.

The effect of initial rotor position estimation error on the start up performance is investigated in Figs. 11, 12, and 13 wherein the machine starts in the interval where $h_a = 1$, $h_b = 0$, and $h_c = 1$. Figs. 11 and 13 display the extreme cases, $\theta_{rh}=3\pi/2$ and $\theta_{rh}=11\pi/6$, in which the estimation error is $\pi/6$. Fig. 12 displays the case where the rotor position is in the center of the interval, $\theta_{rh}=5\pi/3$, and the initial rotor position estimation error is zero. As can be seen, the start up performance is relatively independent of initial rotor position and thus the initial estimation error which results from using the hybrid observer is not a significant disadvantage.

## VI. CONCLUSION

A hybrid observer has been proposed which allows the operation of high-performance sinusoidal type brushless DC machine drives from relatively inexpensive Hall-effect sensors. The performance of the hybrid observer has been demonstrated experimentally and its performance has been shown to compare favorably with that of an optical encoder. It has been sown that the hybrid observer based system performs just as well as an optical encoder based system in the steady-state and nearly as well as the optical encoder during transient conditions. The proposed scheme provides designers with a new option for rotor position sensing, one which offers an excellent compromise between accuracy and cost. Specifically, the hybrid observer has a small but limited error for transient operation but cost much less than an optical encoder or resolver.

## VIII. REFERENCES

[1]    J. P. M. Bahlmann, "A Full-Wave Motor Drive IC Based on the Back EMF Sensing Principle," *IEEE Transactions on Consumer Electronics*, Vol. 35, No. 3, pp. 415-420, August 1989.

[2]    N. Matsui, T. Takeshita, "A Novel Starting Method of Sensorless Salient-Pole Brushless Motor," *Proceedings of the 1994 IAS Conference*, Vol. 1, pp. 386-392, October 1984.

[3]    P. C. Krause, *Analysis of Electric Machinery*, McGraw-Hill, 1986.

[4]    T. W. Nehl, N. A. Demerdash, "Impact of Winding Inductances and other Parameters on the Design and Performance of Brushless DC Motors," *IEEE Transactions on Power Apparatus and Systems*, Vol. PAS-104, pp. 2206-2213, August 1985.

[5]    S. D. Sudhoff, K. A. Corzine, and H. J. Hegner, "A Flux Weakening Strategy for Current-Regulated Surface-Mounted Permanent Magnet Machine Drives," *IEEE Transactions on Energy Conversion*, Vol. 10, No. 3, pp. 431-437, September 1995.

[6]    K. A. Corzine, S. D. Sudhoff, and H. J. Hegner, "Analysis of a Current-Regulated Brushless DC Drive," *IEEE Transactions on Energy Conversion*, Vol. 10, No. 3, pp 438-445, September 1995.

Keith A. Corzine received the BSEE and MSEE degrees from the University of Missouri - Rolla in 1992 and 1994, respectively, and is currently pursuing the Ph.D. degree. His interest include the design and modeling of electric machinery and electric drive systems.

Scott D. Sudhoff received the BSEE, MSEE, and Ph.D. degrees at Purdue University in 1988, 1989, and 1991, respectively. He is currently an Assistant Professor at the University of Missouri - Rolla. His interest include the analysis, simulation, and design of electric machinery, drive systems, and finite-inertia power systems. He has authored or co-authored twelve journal papers in these areas.